Two-dimensional viscoplastic dambreaks

Y. Liu[a], N.J. Balmforth[a,*], S. Hormozi[b], D.R. Hewitt[c]

[a] *Department of Mathematics, University of British Columbia, Vancouver, BC, V6T 1Z2, Canada*
[b] *Department of Mechanical Engineering, Ohio University, Athens, OH, 45701-2979, USA*
[c] *Department of Applied Mathematics and Theoretical Physics, University of Cambridge, CB3 0HA, United Kingdom*

Abstract

We report the results of computations for two-dimensional dambreaks of viscoplastic fluid, focusing on the phenomenology of the collapse, the mode of initial failure, and the final shape of the slump. The volume-of-fluid method is used to evolve the surface of the viscoplastic fluid, and its rheology is captured by either regularizing the viscosity or using an augmented-Lagrangian scheme. We outline a modification to the volume-of-fluid scheme that eliminates resolution problems associated with the no-slip condition applied on the underlying surface. We establish that the regularized and augmented-Lagrangian methods yield comparable results, except for the stress field at the initiation or termination of motion. The numerical results are compared with asymptotic theories valid for relatively shallow or vertically slender flow, with a series of previously reported experiments, and with predictions based on plasticity theory.

1. Introduction

The sudden gravitational collapse of a mass of viscoplastic fluid features in a diverse range of problems from geophysics to engineering. These flows can constitute natural or manmade hazards, as in the disasters caused by mud surges and the collapse of mine tailing deposits. In an industrial setting, the controlled release of a reservoir in a simple dambreak experiment forms the basis of a number of practical rheometers, including the slump test for concrete [1, 2] and the Bostwick consistometer of food science [3]. The slump test features the release of a cylinder of yield-stress fluid. The focus of the current article is more aligned with the Bostwick consistometer, in which materials such as ketchup are released in a rectangular channel, and two-dimensional flow is a convenient idealization. In view of the relatively slow nature of the flows in many of these problems, we also consider the limit of small inertia.

Despite wide-ranging practical application, the theoretical modelling of viscoplastic dambreaks remains relatively unexplored. Asymptotic theories for shallow, slow flow have received previous attention and permit a degree of analytical insight into the problem (see [4, 5] and references therein). Numerical computations of two-dimensional dambreaks have also been conducted to model flows that are not necessarily shallow [6]. However, these simulations do not provide a detailed survey of the flow dynamics over a wide range of physical conditions and have focused mainly on determining some of the more qualitative aspects of the end state of a slump, such as its final runout and maximum depth. Complementing both asymptotics and numerical simulation are cruder predictions of the final shape based on solid mechanics and initial failure criteria derived from plasticity theory [1, 7, 8].

The key feature of a viscoplastic fluid that sets the problem apart from a classical viscous dambreak is the yield stress. When sufficient, this stress can hold the fluid up against gravity, preventing any flow whatsoever. If collapse does occur, the yield stress brings the fluid to a final rest and can maintain localized rigid regions, or "plugs", during the slump. The evolving plugs and their bordering yield surfaces present the main difficulty in theoretical models, particularly in numerical approaches. Augmented-Lagrangian schemes that deal with the complications of the yield stress directly are often time-consuming to run, whereas regularizations of the constitutive law that avoid true yield surfaces introduce their own issues [9]. For the dambreak problem, difficulties are compounded by the need to evolve the fluid surface and impose boundary conditions such as no-slip on the substrate underneath the fluid.

In the current paper, we present numerical computations of viscoplastic dambreaks spanning a wide range of physical parameters. Our aim is to describe more fully the phenomenology of the collapse and its plugs, the form of the motion at initiation, and the detailed final shape. Our main interest is in the effect of the yield stress, so we consider Bingham fluid, ignoring any rate-dependence of the plastic viscosity. We mathematically formulate the dambreak problem in section 2 and outline the numerical strategies we use for its solution. We use both an augmented-Lagrangian scheme and regularization of the constitutive law to account for viscoplasticity; to deal with the free surface, we use the volume-of-fluid method. The latter method emplaces the viscoplastic fluid beneath a

*Corresponding author: *E-mail:* njbmath.ubc.ca, *Telephone:* 604 827 3034

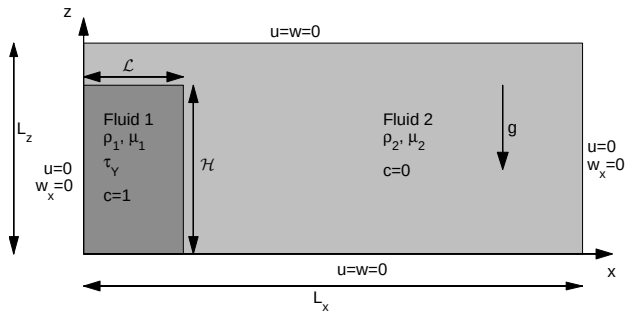

Figure 1: A sketch of the geometry for the case of a rectangular initial block.

less dense and viscous fluid, then tracks the interface between the two using a concentration field. This effectively replaces the single-phase dambreak problem with that of a two-phase miscible fluid displacement (we ignore surface tension), but introduces a significant complication when imposing a no-slip boundary condition: because the lighter fluid cannot be displaced from the lower surface, the slumping heavier fluid over-rides a shallow finger of lighter fluid which lubricates the overlying flow and thins continually, leading to difficulties with resolution. We expose this complication for a viscous test case in section 3, and identify means to avoid it. We then move on to a discussion of Bingham dambreaks in section 4, before concluding in section 5. The appendices contain additional technical details of the numerical schemes, asymptotic theories for shallow or slender flow, and some related plasticity solutions.

2. Formulation

2.1. Dambreak arrangement and solution strategy

To simulate the collapse of a Bingham fluid, we consider a two-fluid arrangement, with the yield-stress fluid emplaced underneath a lighter viscous fluid. We ignore any interfacial tension. The volume-of-fluid method is used to deal with the boundary between the two fluids: a concentration field $c(x, y, t)$ smooths out and tracks the fluid-fluid interface; $c = 1$ represents the viscoplastic fluid and the overlying Newtonian fluid has $c = 0$. The concentration field satisfies the advection equation for a passive scalar; no explicit diffusion is included although some is unavoidable as a result of numerical imprecision. Figure 1 shows a sketch of the geometry; the initial block of viscoplastic fluid has a characteristic height $\mathcal{H}$ and basal width $2\mathcal{L}$, but we assume that the flow remains symmetrical about the block's midline and consider only half of the spatial domain.

To deal with the yield stress of the viscoplastic fluid, we use both an augmented-Lagrangian scheme [10] and a regularization of the Bingham model. The numerical algorithm is implemented in C++ as an application of PELICANS[1]. We refer the reader to [11, 12] for a more detailed description of the numerical method and its implementation. We use the regularized scheme as the main computational tool; the augmented-Lagragian algorithm is slower and was used more sparingly, specifically when looking at flow close to failure or during the final approach to rest. In most situations, the agreement between the two computations is satisfying (examples are given below in figure 4); only at the initiation or cessation of motion is there a noticeable difference, primarily in the stress field (discounting the solution for the plug, which is an artifact of the iteration algorithm in the augmented-Lagrangian scheme).

2.2. Model equations

We quote conservation of mass, concentration and momentum for a two-dimensional incompressible fluid in dimensionless form:

$$\boldsymbol{\nabla \cdot u} = 0, \qquad \frac{\partial c}{\partial t} + (\boldsymbol{u \cdot \nabla})c = 0, \tag{1}$$

$$\rho Re \left[\frac{\partial \boldsymbol{u}}{\partial t} + (\boldsymbol{u \cdot \nabla})\boldsymbol{u}\right] = -\boldsymbol{\nabla} p + \boldsymbol{\nabla \cdot \tau} - \rho \hat{\boldsymbol{z}}, \tag{2}$$

In these equations, lengths $\boldsymbol{x} = (x, z)$ are scaled by the characteristic initial height of the Bingham fluid, $\mathcal{H}$, velocities $\boldsymbol{u} = (u, w)$ by the speed scale $\mathcal{U} = \rho_1 g \mathcal{H}^2/\mu_1$, and time t by $\mathcal{H}/\mathcal{U}$, where g is the gravitational acceleration; the stresses $\boldsymbol{\tau}$ and pressure p are scaled by $\rho_1 g \mathcal{H}$. The Reynolds number is defined as $Re = \rho_1 \mathcal{U}\mathcal{H}/\mu_1$. Here, the subscript 1 or 2 on the (plastic) viscosity μ and density ρ distinguishes the two fluids, and linear interpolation with the concentration field c is used to reconstruct those quantities for the mixture; *i.e.* after scaling with the denser fluid properties,

$$\rho = c + (1 - c)\frac{\rho_2}{\rho_1} \qquad \text{and} \qquad \mu = c + (1 - c)\frac{\mu_2}{\mu_1}. \tag{3}$$

In dimensionless form, the unregularized Bingham constitutive law is

$$\begin{cases} \dot{\gamma}_{jk} = 0, & \tau < cB, \\ \tau_{jk} = \left(\mu + \dfrac{cB}{\dot{\gamma}}\right)\dot{\gamma}_{jk}, & \tau > cB, \end{cases} \qquad \tau = \sqrt{\frac{1}{2}\sum_{j,k} \tau_{jk}^2} \tag{4}$$

where

$$B = \frac{\tau_Y \mathcal{H}}{\mu_1 \mathcal{U}} \equiv \frac{\tau_Y}{\rho_1 g \mathcal{H}} \tag{5}$$

is a dimensionless parameter related to the yield stress τ_Y, and the deformation rates are given by

$$\dot{\gamma}_{jk} = \frac{\partial u_j}{\partial x_k} + \frac{\partial u_k}{\partial x_j}, \qquad \dot{\gamma} = \sqrt{\frac{1}{2}\sum_{j,k} \dot{\gamma}_{jk}^2}. \tag{6}$$

[1] https://gforge.irsn.fr/gf/project/pelicans/; PELICANS is an object-oriented platform developed at the French Institute for Radiological Protection and Nuclear Safety and is distributed under the CeCILL license agreement (http://www.cecill.info/).

The regularized version that we employ is

$$\tau_{jk} = \left(\mu + \frac{cB}{\dot{\gamma} + \epsilon}\right)\dot{\gamma}_{jk}, \tag{7}$$

where ϵ is a small regularization parameter. We verified that the size of this parameter had no discernible effect on the results presented below; we therefore consider irrelevant the precise form of the regularization (which is simple, but not necessarily optimal).

We solve these equations over the domain $0 \le x \le \ell_x = L_x/\mathcal{H}$ and $0 \le z \le \ell_z = L_z/\mathcal{H}$, and subject to no-slip conditions, $u = w = 0$ on the top and bottom surfaces (but see §3), and symmetry conditions on the left and right edges, $u = 0$ and $w_x = 0$. The computational domain is chosen sufficiently larger than the initial shape of Bingham fluid that the precise locations of the upper and right-hand boundaries (*i.e.* ℓ_x and ℓ_z) exert little effect on the flow dynamics.

Initially, both fluids are motionless, $u(x, z, 0) = w(x, z, 0) = 0$. We take the initial shape of the viscoplastic fluid to be either a block or triangle; the concentration field then begins with

$$c(x, z, 0) = 1 \text{ for } \begin{cases} 0 \le x \le X_0 \text{ or } X_0(1 - \frac{1}{2}z), \\ 0 \le z \le 1 \text{ or } 2, \end{cases}$$

and $c(x, z, 0) = 0$ elsewhere, where $X_0 = \mathcal{L}/\mathcal{H}$ is the initial aspect ratio. The different maximum depths ensure that the initial conditions have the same area for equal basal width X_0.

The main dimensionless parameters that we vary are the yield-stress parameter B (which we loosely refer to as a Bingham number) and initial aspect ratio X_0. Unless otherwise stated, we set the other parameters to be

$$\ell_x = 5, \quad \ell_z = 1.25, \quad \frac{\rho_2}{\rho_1} = \frac{\mu_2}{\mu_1} = Re = 10^{-3}.$$

By fixing the density and viscosity ratios to be small, we attempted to minimize the effect of the overlying viscous fluid (but see the discussion of the finger of over-ridden fluid below). The relatively low Reynolds number reflects our interest in the limit of small inertia, although the PELICANS implementation requires $Re \neq 0$, evolving the fluid from the motionless state; we established that adopting $Re = 10^{-3}$ minimizes the effect of inertia beyond the initial transient. Some additional technical details of the computations are summarized in Appendix A. In this appendix, we also describe a second scheme that we used to study how the initial state fails at $t = 0$; this scheme does not solve the initial-value problem, but calculates the instantaneous velocity field at $t = 0$, assuming that $Re = 0$ and the initial stresses are in balance (the steady Stokes problem).

3. Newtonian benchmark

The collapse of the initial block of the heavier viscous fluid creates a slumping current that flows out above the bottom surface. However, because of the no-slip condition imposed there, the upper-layer fluid cannot be displaced from a thin finger coating the base that is over-ridden by the advancing gravity current. Problematically, the finger becomes excessively thin and difficult to resolve with the relatively small viscosity and density ratios that we used to minimize the effect of the lighter fluid. We illustrate the formation of the finger and its subsequent development in figure 2. Appendix A features further discussion of the finger and its evolution.

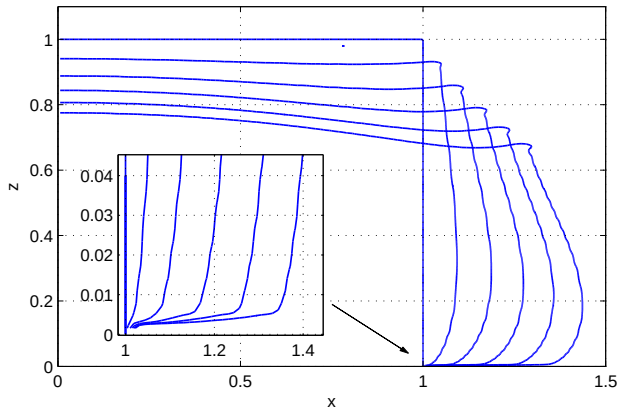

Figure 2: Snapshots of the evolving interface for a Newtonian heavier fluid at the times $t = 1, 2, 3, 4, 5$; the inset shows a magnification of the finger of over-ridden lighter fluid.

The challenges associated with resolving the finger are illustrated in figure 3, which plots the evolution in time of the flow front, $X(t)$ (defined as the rightmost position where $c(X, z, t) = \frac{1}{2}$), for computations with different grid spacing. The first panel in this figure shows the results using a relatively simple MUSCL scheme for tracking the interface [13], which was previously coded into PELICANS [11, 12]. This algorithm fails to track the interface well with the grid resolutions used: as the finger develops, it remains erroneously thick and the enhanced lubrication by the lighter viscous fluid causes the heavier current to advance too quickly (*cf.* Appendix A.3).

An interface-tracking scheme based on the PLIC algorithm proposed in [14] performs better; see figure 3(b). The flow front now advances less quickly. However, the fine scale of the finger still leads to a relatively slow convergence of the computations with grid spacing $\Delta x = \Delta z$ (corresponding to finite elements in the PELICANS code with equal aspect ratio). Moreover, the resolution failure is again manifest as an enhancement in the runout of the current that results from a finger that does not thin sufficiently quickly. In Appendix A.3 we argue that this is an intrinsic feature of the volume-of-fluid algorithm when the interface is contained within the lowest grid cell of the numerical scheme.

The resolution problems with the finger are compounded in computations with Bingham fluid, for which the yield stress further decreases the effective viscosity ratio. Al-

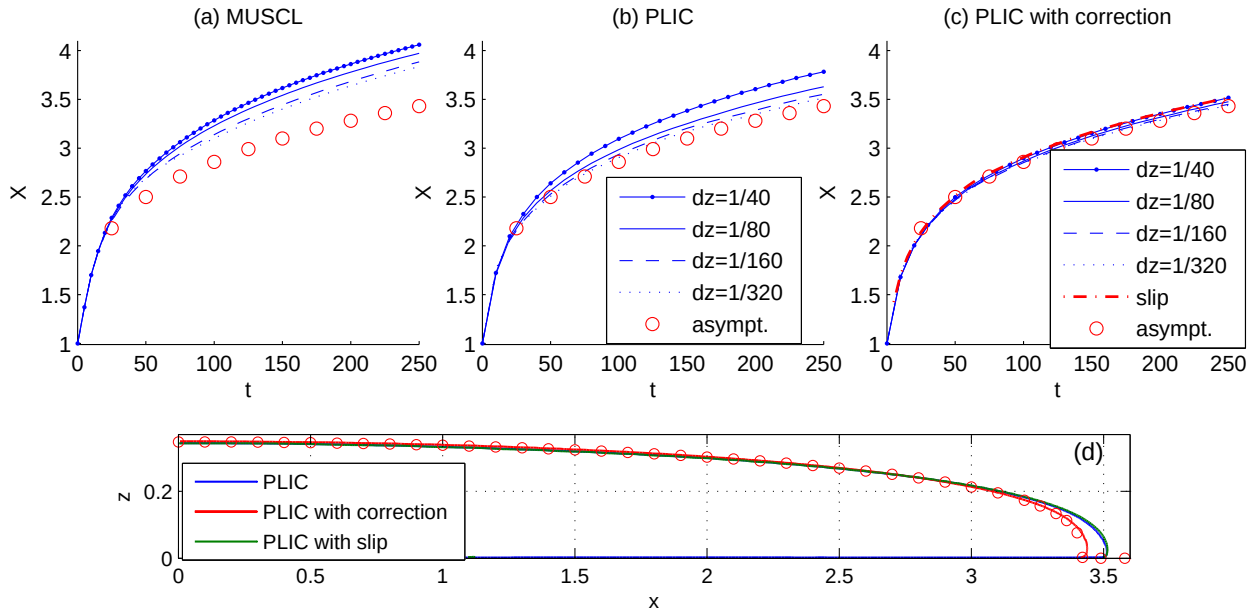

Figure 3: Flow front $X(t)$ plotted against time for computations with Newtonian fluids using (a) the simple MUSCL scheme, (b) the PLIC improvement, and (c) the PLIC scheme with the lower boundary condition on $c(x, z, t)$ adjusted according to the algorithm outlined in the main text. In each case, runs with different resolution are shown. For (c), the (red) dashed-dotted line labelled *slip* shows a solution computed with the PLIC scheme, but with no slip imposed on the heavier fluid and free slip imposed on the lighter fluid at $z = 0$. The circles show the prediction of the leading-order, shallow-layer asymptotics in Appendix B. In (d), we plot the interface shape at $t = 250$ for the highest resolution solutions computed with the PLIC scheme with the three different lower boundary conditions.

though some sort of local mesh refinement and adaptation would be a natural way to help counter these problems, we elected to avoid them in a different fashion which was more easily incorporated into PELICANS. In particular, by monitoring $c(x, z, t)$ at $z = \Delta z$ for each time step, we determined when the finger was expected to be contained within the lowest grid cell. At this stage, to prevent the resolution failure from artificially restricting the thinning of the finger in the volume-of-fluid scheme (see Appendix A.3), we reset the concentration field to $c = 1$ at $z = 0$. The finger was thereby truncated and the effective contact line moved. Practically, we reset $c(x, 0, t)$ when $c(x, \Delta z, t)$ exceeded 0.99 (the results were insensitive to the exact choice for this value). As shown by figure 3(c), this led to computations that converged much more quickly with grid spacing and fell close to both the most highly resolved computations with the original PLIC scheme and the predictions of shallow-layer theory. Nevertheless, the adjustment destroys the ability of the code to preserve the volumes of the two fluids. For the computations we report here, less than about one percent of the volume of the lighter fluid was lost as a result of the adjustment. But, as the velocity profile was then fully resolved near the boundary and no other unexpected problems were found, we considered this flaw to be acceptable. Hereon, all reported computations use this adjusted boundary condition.

To provide a physical basis of the adjustment scheme, we would need to demonstrate that it corresponds to the addition of another physical effect, such as van der Waals interactions. We did not do this here, but simply note that the adjustment acts like the numerical devices implemented in contact line problems with surface tension to alleviate the stress singularity and allow the contact line to move [15]. Indeed, the scheme is much like limiting the dynamic contact angle to be about $3\pi/4$ or less, by adjusting the interface over the scale of the bottom grid cell but without introducing explicitly any interfacial tension.

An alternative strategy is to change the lower boundary condition so that the lighter fluid freely slips over the lower surface whilst the heavier fluid still satisfies no slip. This strategy, which can be incorporated using a Navier-type slip law in which the slip length depends on c, leads to results that compare well with the scheme including the concentration correction (see figure 3(c)). However, for Bingham fluid, the diffuse nature of the interface-tracking scheme and the PLIC algorithm eventually result in the recurrence of resolution problems over longer times. By contrast, the adjustment scheme successfully survives the long time diffusion process.

4. Bingham slumps

For the collapse of a Bingham fluid, we first describe the general phenomenology, then explore the details of failure, and finally categorize the slumped end-states. Along the way, we indicate how the computations approach the asymptotic limits of relatively shallow (low, squat) or slender (tall, thin) slumps.

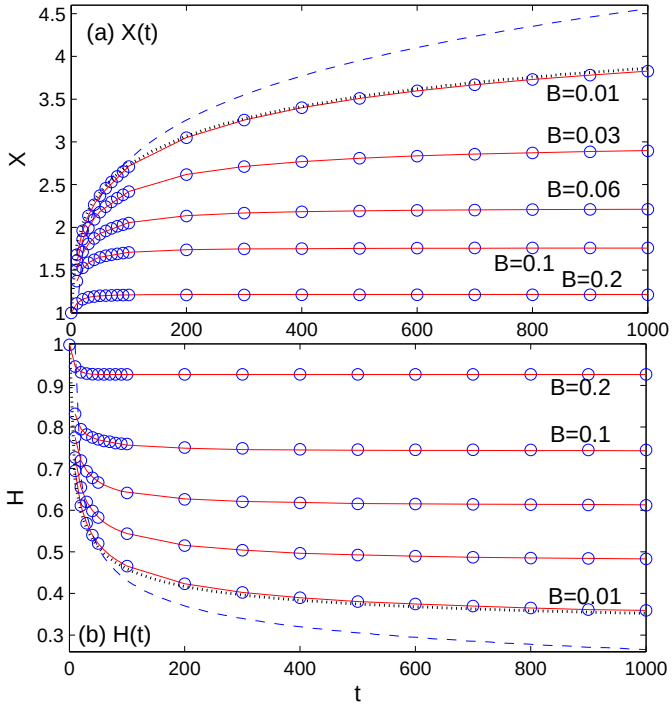

Figure 4: (a) Front position $X(t)$ and (b) central depth $H(t) = h(0, t)$ for Bingham dambreaks with a square initial block ($X_0 = 1$) and the values of B indicated. The dashed lines show the Newtonian results. For the viscoplastic cases, the circles show the result using the augmented-Lagrangian scheme and the lines indicate the result with a regularized constitutive law. The dotted lines show the prediction of the leading-order shallow-layer asymptotics for $B = 0.01$.

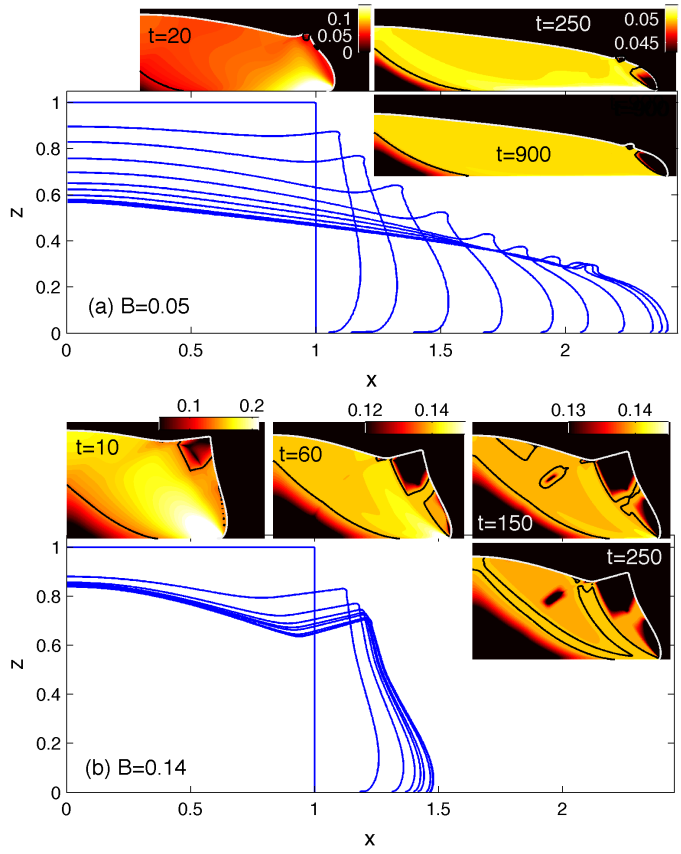

Figure 5: Snapshots of a collapsing square with (a) $B = 0.05$ at $t = 0$, 2.5, 5, 10, 20, 40, 70, 150, 450, 950, 4000, and (b) $B = 0.14$ at $t = 0$, 10, 50, 100, 200, ..., 1000. The insets show density plots of the stress invariant τ at the times indicated, with the yield surfaces drawn as solid lines (and common shading maps for the final two snapshots in each case).

4.1. Slump and plug phenomenology

When the heavier fluid is viscoplastic, collapse only occurs provided the yield stress does not exceed a critical value B_c that depends on initial geometry. For $B < B_c$, the viscoplastic fluid collapses, but the yield stress eventually brings the flow to an almost complete halt (slumps with the regularized constitutive law never truly come to rest, and iteration errors in the augmented-Lagrangian scheme prevent the velocity field from vanishing identically). Figure 4 plots the position of the flow front $X(t)$ and central depth $H(t) = h(0, t)$ for computations with varying B, beginning from a square ($X_0 = 1$) initial block. For this shape, the critical value below which collapse occurs is $B_c \approx 0.265$, and unlike the inexorable advance of the Newtonian current (shown by a dashed line), $X(t)$ and $H(t)$ eventually converge to $B-$dependent constants (the case with the smallest $B = 0.01$ requires a longer computational time than is shown).

Sample collapses from square blocks with $B = 0.05$ and 0.14 are illustrated in more detail in figure 5. The first example shows a slump with relatively low yield stress, for which the fluid collapses into a shallow current. The case with higher B collapses less far, with an obvious imprint left by the initial shape. Note the stress concentration that arises for earlier times in the vicinity of the contact line (a feature of all the slumps, irrespective of initial condition and rheology).

In general, for rectangular initial blocks with order one initial aspect ratio, we find that the flow features two different plug regions during the initial stages of collapse (*cf.* [6]). First, at the centre of the fluid the stresses never become sufficient to yield the fluid, and a rigid core persists throughout the evolution. Second, the top outer corner is not sufficiently stressed to move at the initiation of motion. This feature falls and rotates rigidly as fluid collapses underneath, but eventually liquifies and disappears for small B; at higher yield stress, the rigid corner survives the fall and decorates the final deposit. As the fluid approaches its final shape and flow subsides, further plugs appear, particularly near the flow front; for the deeper final deposits, these plugs appear to thicken and merge to leave relatively thin yielded zones.

When the initial shape is a triangle with $X_0 = O(1)$, only a few of the phenomenological details change (figure 6): the apex of the triangle now falls rigidly as material spreads out underneath; this pinnacle decorates the final deposit unless the yield stress is sufficiently small. Again,

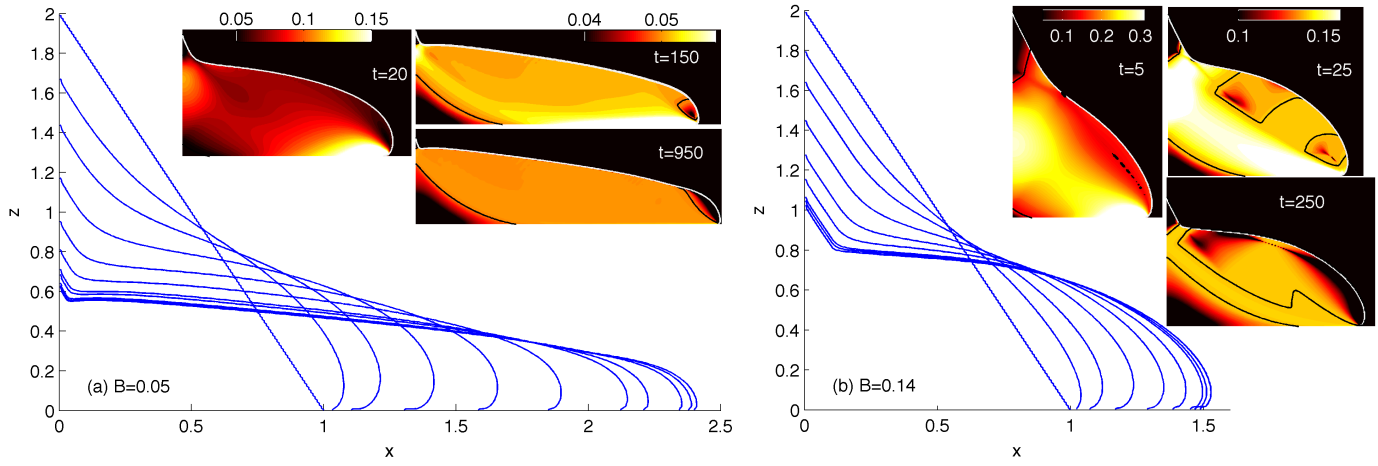

Figure 6: Snapshots of the evolving interface for a triangular initial condition with $X_0 = 1$ and (a) $B = 0.05$ and (b) $B = 0.14$, at $t = 0$, 2.5, 5, 10, 20, 40, 100, 150, 450, 950, 4000. The insets show density plots of the stress invariant τ at the times indicated, with the yield surfaces drawn as solid lines (the two later time density plots have a common shading scheme).

the slump features a rigid core and further plugs form near the nose over late times.

With a relatively wide initial condition, the pattern of evolution is slightly different: for the rectangle, the central rigid plug extends over the entire depth of the fluid layer and only the side of the block collapses. The final deposit then features a flat top at its centre, as illustrated in figure 7(a). Such *incomplete slumps* are predicted by shallow-layer theory to occur for $3BX_0 > 1$ [3]. This estimate can be improved to $3BX_0 > 1 - 3\pi B/4$ using the higher-order theory outlined in Appendix B (and specifically the final-shape formula (9)), which adequately reproduces numerical results for $B < 0.15$; at higher B, the computations indicate that BX_0 must exceed 0.25 ± 0.015 for the slump to preserve a rigid central block

Incomplete slumps of a different kind arise for an initial triangle. In this case, collapses begin over the central regions where the initial stresses are largest, and may not reach the edge, where fluid is initially unyielded, if the triangle is too wide. The (leading-order) shallow-layer model predicts that collapse occurs but does not reach the fluid edge at $x = X_0$ if $4 > BX_0 > 9/8$. As illustrated in figure 7(b), such incomplete slumps are also observed numerically, though again for a slightly different range of initial widths (the plugged toe of the triangle is relatively small in the example shown).

Slender (*i.e.* tall, thin) initial blocks, with $X_0 \ll 1$, also collapse somewhat differently, with fluid yielding only at the base of the fluid and remaining rigid in an overlying solid cap; see figure 8, which shows computations for rectangles (slender triangular slumps are much the same). The lower section of the column subsequently spreads outwards with the rigid cap descending above it in a manner reminiscent of the (axisymmetrical) slump test [1, 2]. Interestingly, the slender slump also generates undulations in the thickness of the column. As illustrated by figure 8(a), these undulations (which do not occur in the Newtonian

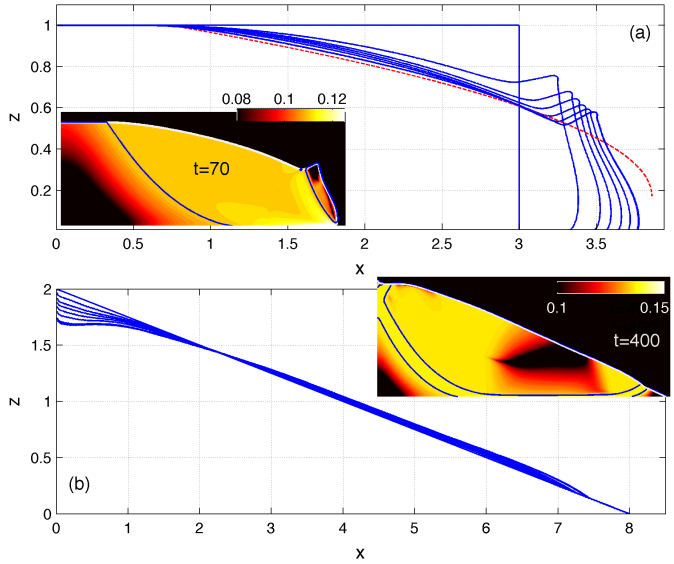

Figure 7: Snapshots of the evolving interface for an initial (a) rectangular with $(X_0, B) = (3, 0.11)$, and (b) triangle with $(X_0, B) = (8, 0.14)$, at the times $t = 0$, 10, 20, 30, 50, 100, 400, 700, 1000. The dotted line in (a) shows a modification of the prediction in (9) that incorporates the central plug (and which terminates at finite height). The insets show density plots of the stress invariant τ at the times indicated, with the yield surfaces drawn as solid lines.

problem) appear towards the end of the collapse and are linked to zigzag patterns in the stress invariant and yield surfaces. The features follow characteristic curves of the stress field (the "sliplines") that intersect the side free surface, and which have slopes close to fortyfive degrees (see Appendix D.1); the wavelength of the pattern is therefore approximately the width of the column.

4.2. Shallow flow

As illustrated above, when $B \ll 1$ the fluid collapses into a shallow current with $|\partial h/\partial x| \ll 1$ whatever the

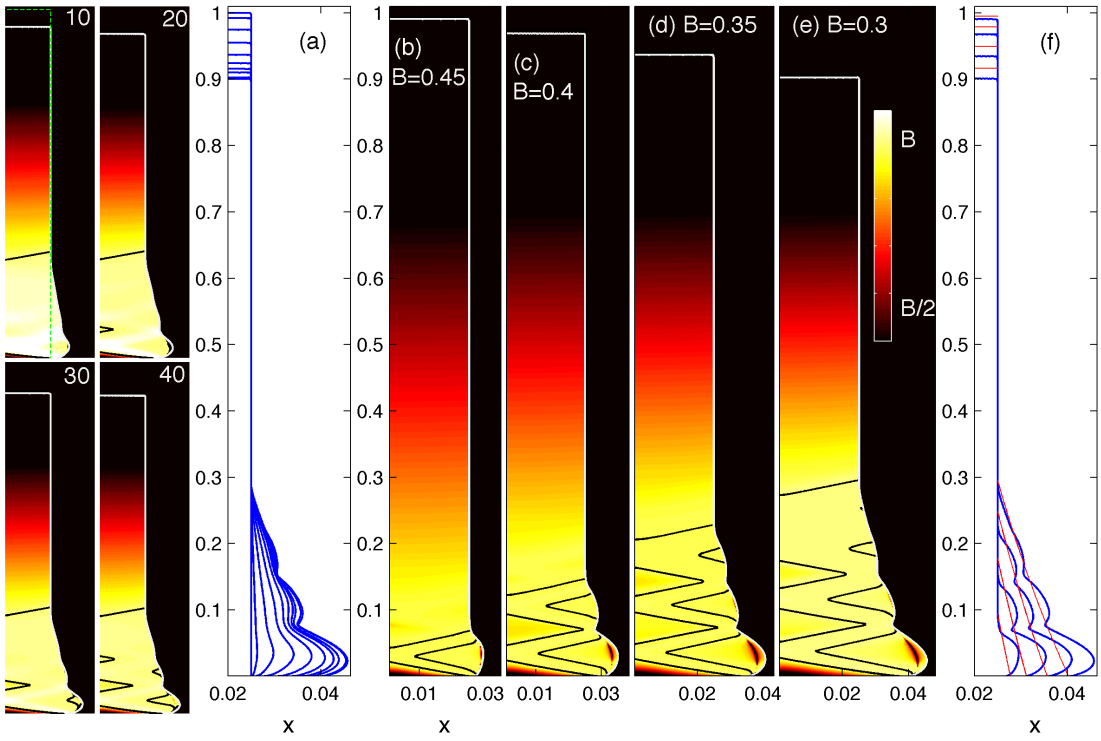

Figure 8: Slumps of slender columns: the four images on the left show collapsing columns for $B = 0.3$ and $X_0 = 0.025$ at the times indicated in the top right corner. Shown are the interface, yield surfaces and colormap of the stress invariant τ. The evolving side profile for this collapse is shown in panel (a) at the times $t = 0$, 4, 9, 16, 25, 36, 49, 100, 400, 1000. Panels (b)–(e) show columns at $t = 50$ for the values of B indicated, all with $X_0 = 0.025$. Panel (f) compares the final side profiles (blue) with the predictions of slender asymptotics (red). The shading scheme for τ for all the colormaps is shown in (e).

initial condition. Asymptotic theory [4, 5] then provides a complementary approach to the problem. As illustrated in figure 4, the sample collapse with $B = 0.01$ is relatively shallow and the numerical solutions for the runout and central depth match the predictions of the shallow-layer asymptotics.

The asymptotics also predicts that flow becomes plug-like over a region underneath the interface (see [16] and Appendix B). This "pseudo-plug" is not truly rigid but is weakly yielded and rides above a more strongly sheared lower layer. Horizontal velocity profiles for a collapsing square block with $B = 0.01$ are shown in figure 9(a) and compared with the predictions of the shallow-layer theory. Although the pseudo-plugs are less obvious in the numerical profiles, the horizontal velocity does become relatively uniform over the predicted pseudo-plug. Figure 9(b) illustrates how the superficial weak deformation rates associated with the pseudo-plug feature in a snapshot of $\log_{10}\dot{\gamma}$, and how the transition to a more obviously sheared layer underneath approximately follows asymptotic predictions.

Nevertheless, the numerical computations show notable disagreements with the shallow-layer asymptotics. None of the true plugs appear in the asymptotic solution, reflecting how they are associated with non-shallow flow dynamics: at the midline, the asymptotics fails to incorporate properly the symmetry conditions, and at the flow front and the relic of the upper right corner, the surface always remains too steep for a shallow approximation. The depth profiles predicted by the asymptotics consequently do not show any of the finer secondary features imprinted by the true plugs, as illustrated by the profile for $B = 0.05$ also plotted in figure 9(c). Only when B is smaller are such features largely eliminated by the fluid flow and the final shape well predicted by the asymptotics.

Despite these details, the broad features of the numerical solutions are reproduced by the shallow-layer asymptotics, particularly when first-order-correction terms are included: for the final shape and if the initial block collapses completely, the leading-order solution is

$$h(x) = \sqrt{2B(X_\infty - x)}; \tag{8}$$

with the next-order corrections, we find

$$h = \sqrt{2B(X_\infty - x)} + \frac{\pi}{2}B \tag{9}$$

(Appendix B). The final runout X_∞, or slump length, is dictated by matching the profile's area with that of the initial condition. This implies $X_\infty = (9X_0^2/8B)^{1/3}$ for (8) and furnishes an algebraic problem to solve in the case of (9), with approximate solution $X_\infty \approx (9X_0^2/8B)^{1/3}[1 - \pi(B^2/81X_0)^{1/3}]$. As shown in figure 9(c), the prediction (9) agrees well with the shapes reached at the end of the numerical computations, even though the profile ends in a vertical cliff which violates the shallow-layer asymptotics.

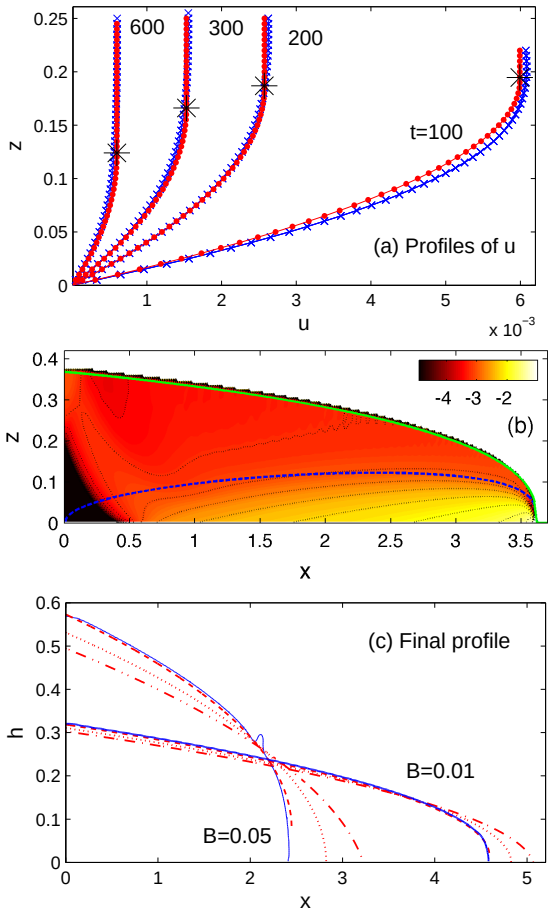

Figure 9: Comparison of shallow-layer theory with numerical results for a collapsing square block ($X_0 = 1$) with $B = 0.01$: (a) Horizontal velocity profiles at $x = 2.5$ and the times indicated. (b) Logarithmic strain-rate invariant, A density map of $\log_{10}\dot{\gamma}$ on the $(x, z)-$plane, at $t = 600$. (c) Final shape. In (a) the crosses plot the numerical solution, and the points indicate the asymptotic profile (B.2); the star locates the bottom of the pseudo-plug. In (b), the solid (green) and dashed (blue) lines show the surface and fake yield surface ($z = Y = h + B/h_x$) predicted by asymptotics. In (c), the final profile for $B = 0.05$ is included. The solid lines show computed final states, the dotted lines denote the leading-order result (8) and the dashed line shows the higher-order prediction (9). The dashed-dotted line is the asymptotic prediction (13) from [17].

4.3. Slender slumps

For a slender column with $X_0 \ll 1$, we can again make use of the small aspect ratio to construct an asymptotic solution. As summarized in Appendix C, this limit corresponds to theory of slender viscoplastic filaments [18] and indicates that the final state is given by

$$x = \xi(z) = \frac{X_0}{2B}\exp\left(-\frac{z}{2B}\right) \quad \text{for } 0 \le z \le Z, \tag{10}$$

where

$$Z = -2Bh(0,0)\log(2B) \tag{11}$$

is the height dividing yielded fluid from the overlying rigid plug. The fluid adopts its original shape over $Z < z < Z + 2Bh(0,0)$, having fallen a vertical distance $(1-2B)h(0,0) - Z$. It follows that the column will not slump if $B > \frac{1}{2}$,

$$X_\infty = \frac{X_0}{2B} \qquad \text{and} \qquad H_\infty = 2Bh(0,0)[1 - \log(2B)]. \tag{12}$$

The latter is equivalent to the "dimensionless slump" reported previously [1, 2], although it was not declared as an asymptotic result relying on the column being slender. The profile (10) is compared with the final profiles of numerical computations in figure 8. Aside from the relatively short-wavelength undulations in column thickness over the yielded base of the fluid (whose lengthscale violates the slender approximation), the asymptotics are in broad agreement with the numerical results.

Note that overly slender configurations are likely susceptible to a symmetry-breaking instability in which the column topples over to one side [19]. This is ruled out here in view of our imposition of symmetry conditions along the centreline $x = 0$.

4.4. Failure

4.4.1. Critical yield stress

The critical yield stress, B_c, above which the fluid does not collapse is plotted against initial width, X_0, in figure 10(a) for rectangular initial blocks. We calculate B_c in two ways: first, the final runout X_∞ recorded in the slumps computed with the PELICANS software (defined as in §4.5) converges linearly to the initial width X_0 as $B \to B_c$. Second, in the inertialess problem, the initial stresses dictate the initial velocity field, and the maximum speed also falls linearly to zero as $B \to B_c$. Hence, we can determine B_c without performing any time stepping using the scheme for $Re = 0$ described in Appendix A.2.

As illustrated in figure 10(a), $B_c \approx 0.2646$ independently of X_0 when $X_0 > 1$. For such initial widths, collapses are incomplete and a solid core spans the full depth of the fluid, rendering the failure criterion independent of X_0. The initial width matters for $X_0 < 1$, leading to an increase of B_c. Eventually, $B_c \to \frac{1}{2}$ for $X_0 \to 0$, as expected from the slender column asymptotics in §4.3.

Just below the critical yield stress, velocities are small and the Bingham problem reduces to an analogous one in plasticity theory except over thin viscoplastic boundary layers. The incomplete slump is analogous to the classical geotechnical problem of the stability of a vertical embankment (*e.g.* [23]), provided no deformation occurs in $z < 0$. Classical arguments dating back to Coulomb, describe the form of failure in terms of the appearance of a slip surface dividing rigid blocks, allowing analytical estimations of B_c from balancing the plastic dissipation across the slip surface with the potential energy release. In particular, assuming that the failure occurs by the rotation of the top right corner above a circular arc, one arrives at an estimate $B_c \approx 0.261$, after maximizing over all possible positions of the centre of rotation (*cf.* [24] and figure 11(a)). However, this type of solution strictly provides only a lower bound

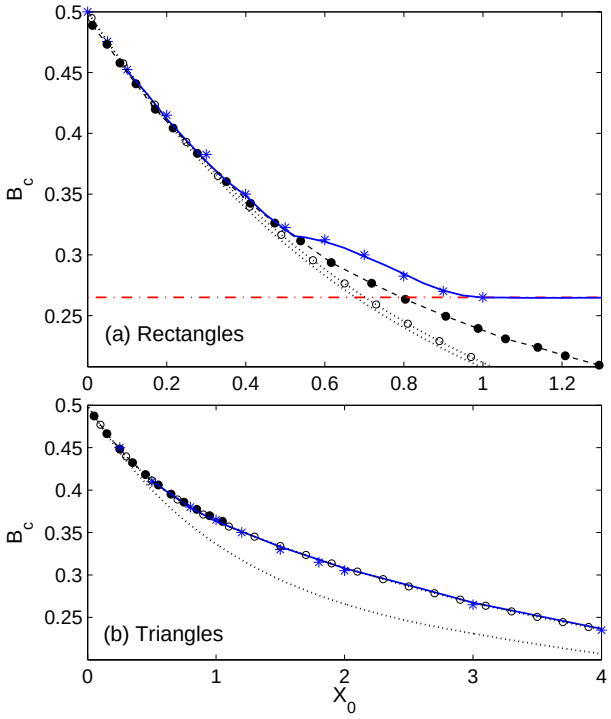

Figure 10: Critical yield stress, B_c, plotted against initial width X_0 for (a) rectangular and (b) triangular blocks, found by from monitoring either the final runout X_∞ (stars) or the initial maximum speed for $Re = 0$ (solid line). In (a), also shown are the bounds $B_c = 0.2642$ and 0.2651 obtained from plastic limit-point analysis [20, 21, 22] (dashed-dotted), results from slip-line theory [7] (dashed line with points) and the simple lower bound $B_c = \frac{1}{2}(\sqrt{X_0^2+1}-X_0)$ [8] (dotted line). The analogues of the latter two for the triangular blocks (see Appendix D) are shown in (b). The dotted lines with open circles show improvements of the simple lower bounds allowing for rotational failure (see Appendix D.2).

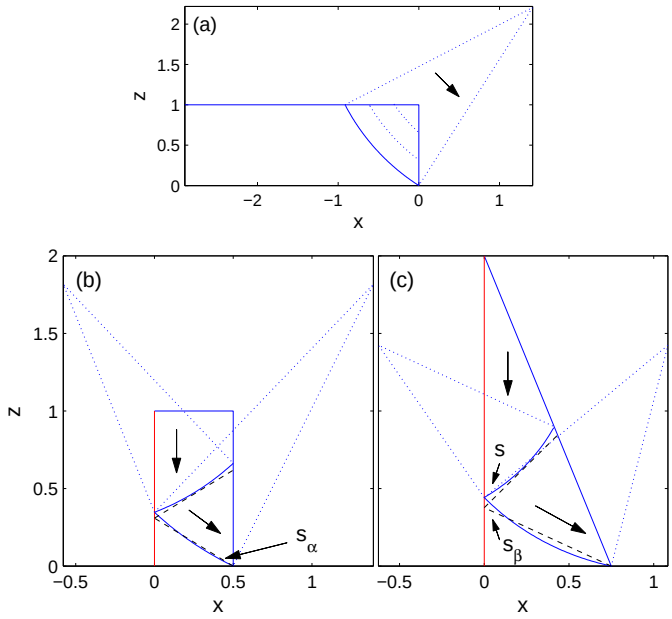

Figure 11: Trial velocity fields to compute lower bounds on B_c for (a) the vertical embankment with a circular slip curve, and relatively slender (b) rectangular and (c) triangular initial blocks. In (b) and (c), the straight (dashed) and circular (solid) failure surfaces for linear or rotational sliding motion are plotted; these surface can be parametrized by the local slopes at the bottom corner, s_α, and midline, s_β and s (for linear sliding $s_\alpha = s_\beta$).

on B_c and may not be the actual mode of failure. Indeed, the bound has been optimized and improved to 0.2642, and a complementary upper bound computed to be 0.2651 [20, 21, 22]; the optimization suggests that failure occurs over a relatively wide region of plastic deformation [21]. The upper and lower bounds are included in figure 10(a), and are indistinguishable on the scale of this picture, but bracket the value of $B_c \approx 0.2646$ found for our Bingham slumps with $X_0 > 1$.

For a slender column, Chamberlain *et al.* [8] provide an estimate of the critical yield stress by assuming that two lines of failure occur: the lowest cuts off a triangular basal section, whereas the upper cleaves off a second triangle that slides away sideways, leaving the remaining overlying trapezoid to fall vertically; see figure 11(b). Optimizing the slopes of the two cuts furnishes the lower bound, $B_c = \frac{1}{2}(\sqrt{1+X_0^2} - X_0)$, which is included in figure 10. Chamberlain *et al.* [7] also provide a numerical solution of the slipline field for a failure with the form of an unconfined plastic deformation. This estimate converges towards their lower bound as $X_0 \to 0$, as indicated in figure 10(a). Our numerically determined values of B_c match Chamberlain *et al.*'s slipline solutions for $X_0 < 0.5$. For wider initial blocks, the slipline solutions deviate from the numerical results and become inconsistent with the bounds for the vertical embankment for $X_0 > 0.8$, highlighting how a different failure mechanism must operate.

For triangles, no corresponding plasticity solutions exist in the literature. However, Chamberlain *et al.*'s [7, 8] slipline solution and simple lower bound can easily be generalized, as outlined in Appendix D and illustrated in figure 11(c). The slipline solution and bound are compared with numerical data in figure 10(b). Again, $B_c \to \frac{1}{2}$ for $X_0 \to 0$. Now, however, the slope of the initial free surface continues to decline as X_0 is increased, and so there is no convergence to a limit that is independent of width. Instead, the shallow layer theory of Appendix B becomes relevant and predicts that $B_c \to 4/X_0$ for $X_0 \gg 1$ (a limit lying well beyond the numerical data in figure 10(b)).

Note that Chamberlain *et al.*'s lower bounds can be improved by allowing the triangle at the side to rotate out of position rather than slide linearly; see Appendix D.2. The failure surfaces then become circular arcs, as illustrated in figure 11(b,c). For the rectangle, the resulting improvement in the bound on B_c amounts to a few percent and is barely noticeable in figure 10(a). More significant is the improvement of the bound for the triangle, which is brought much closer to the numerical and plasticity results; see figure 10(b).

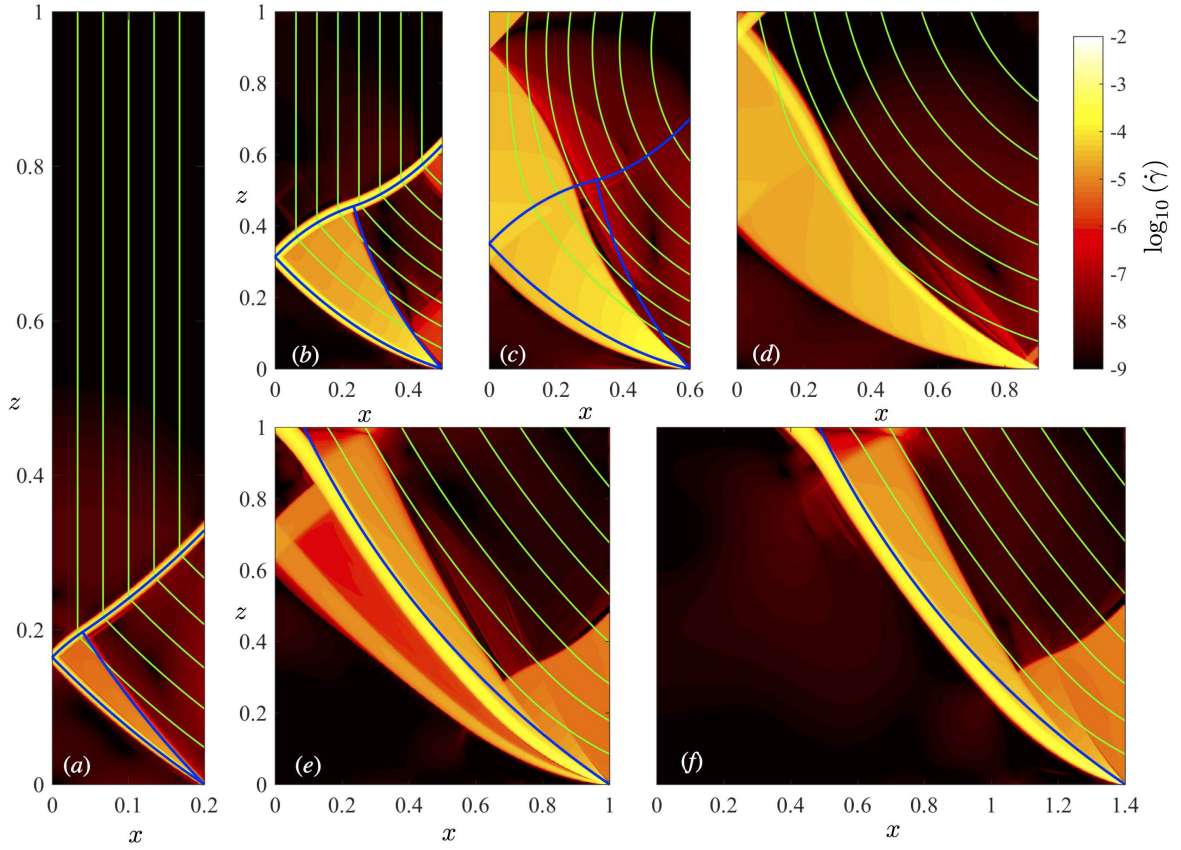

Figure 12: Strain-rate invariant plotted logarithmically as a density on the $(x, z)-$plane for solutions with $B = 0.99B_C$ and $t = Re = 0$ (Appendix A.2), at the values of X_0 indicated by the $x-$axis. Also shown are a selection of streamlines. In (a)–(c), the solid blue lines indicate the border of the plastic region and expansion fan of the corresponding slipline solutions (Appendix D). In (e) and (f), the blue lines indicate the circular failure surface of the lower bound solution.

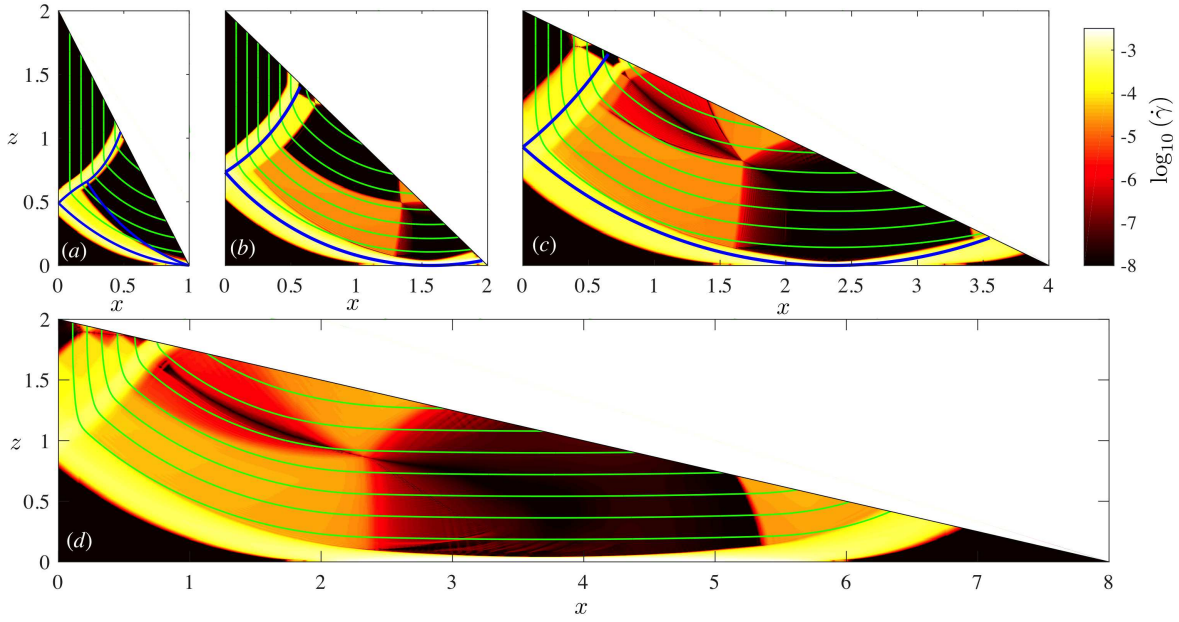

Figure 13: A series of pictures similar to figure 12, but for initial triangles (with solid blue lines showing the yield surfaces of the slipline solution in (a), and the circular arcs of the bound of Appendix D.2 for rotational failure in (b) and (c)).

4.4.2. Flow at failure

The failure modes of our rectangular viscoplastic solutions (for $t = Re = 0$) are illustrated in figure 12. The thinner initial columns yield only over a triangular shaped region at the base which closely matches that predicted by slipline theory [7] (see also Appendix D.1). The failure mode changes abruptly when X_0 slightly exceeds about 0.5. The failure zone then takes the form of a widening wedge extending from the lower left corner of the initial block up to the centre of the top, with the entire side face remaining rigid. Evidently, this mode of failure is preferred over the slipline solution at these values of X_0, leading to the departure of the observed values of B_c from Chamberlain *et al.*'s curve in figure 10(a). The failure mode changes a second time for $X_0 \approx 1$: wider initial blocks fail chiefly over a relatively narrow layer connecting the lower left corner to an off-centre location on the top surface, which lies close to the circular failure surface of the simple lower bound in figure 11(a).

For both the narrower and wider examples in figure 12, the failing deformations are dominated by sharp viscoplastic boundary layers that likely correspond to yield surfaces. Spatially extensive regions (in comparison to the fluid depth or width) of plastic deformation do, nevertheless, occur, and the failure modes never take the form of a patchwork of sliding rigid blocks. Note that it is difficult to cleanly extract the yield surfaces as $B \to B_c$, which complicates the identification of the failure mode. In figure 12, we have avoided showing these surfaces and instead displayed the deformation rate and a selection of streamlines. Curiously, for $X_0 > 0.5$, it is difficult to envision how one might construct corresponding slipline fields (there are no surfaces bounding the plastic zone with known stresses that can be used to begin the slipline construction).

For a triangular initial condition, failure for smaller widths again occurs through the appearance of a lower plastic zone that compares well with slipline theory; see figure 13. This agreement is confirmed by the match of the observed critical yield stress, $B_c(X_0)$, with the slipline predictions in figure 10(b). Unlike the rectangle, however, there is no abrupt change in failure mode as X_0 is increased, at least until the surface slope of the triangle becomes too shallow to apply Chamberlain *et al.*'s construction [7] (see Appendix D.1). At the largest widths, the triangle fails at the centre but not the edge, as already noted in section 4.1.

4.5. The final shape and slump statistics

To extract statistics of the final shape, we define a stopping criterion according to when the stress invariant first becomes equal or less than B at each point in the domain. The resulting "final state" appears to be reached in a finite time (for both augmented-Lagrangian and regularized computations), in disagreement with asymptotic theory [25], which predicts that flow halts only after an infinite time (see also Appendix C). A selection of final profiles for varying Bingham number is displayed in figure 14 for both square and triangular initial conditions.

Plasticity theory is again relevant in the limit that the slump approaches its final state. This fact was used previously [17] to construct the final profiles with slipline theory, following earlier work by Nye [26]. A key assumption of this construction is that the flow is under horizontal compression. The assumption can also be used to continue the shallow-layer asymptotics to higher order to predict the final profile,

$$h = \sqrt{2B(X_\infty - x) + \frac{\pi^2}{4}B^2} - \frac{\pi}{2}B, \qquad (13)$$

which agrees well with the slipline theory [17]. Unfortunately, neither the slipline profiles or (13) compare well with laboratory experiments.

A sample final state from the numerical computations with a diagnosis of the associated slipline field is displayed in figure 15. For the latter, we map out curves of constant $p - z \pm 2B\theta$, which are the invariants that are conserved along the two families of sliplines, where $\theta = -\frac{1}{2}\tan^{-1}(\tau_{xx}/\tau_{xz})$ [27] (see also Appendix D.1). As also shown by figure 15(d), the resulting curves compare well with an explicit computation of sliplines launched from the surface position predicted by (9), where $p = 0$ and the sliplines make an angle $\pi/4$ with the local surface tangent.

The sliplines in figure 15 follow a different pattern to Nye's construction (see figures 5 and 6 in [17]). The reason for this discrepancy is that almost all of our slumps comes to rest in a state of horizontal expansion, rather than compression (we have observed regions under horizontal compression only in the slumps of relatively wide triangles, as in figure 7(b)). Correcting this feature of the dynamics leads to the revised higher-order asymptotics summarized in Appendix B, which culminates in the prediction for the final profile in (9). As is evident from figure 9(c), the asymptotic predictions for horizontal expansion compare much more favourably with the numerical results than the slipline theory and asymptotics for horizontal compression.

The comparison is illustrated further in figure 16, which shows scaled final runouts and depths, $X_\infty/\sqrt{X_0}$ and $H_\infty/\sqrt{X_0}$, as functions of $B/\sqrt{X_0}$ for the numerical computations, slipline theory and the various versions of the shallow-layer asymptotics. Scaling the runout and depth in this fashion corresponds to choosing the initial area as the lengthscale in the non-dimensionalization of the problem. The slipline theory and various versions of the shallow-layer asymptotics furnish curves of $X_\infty/\sqrt{X_0}$ and $H_\infty/\sqrt{X_0}$ against $B/\sqrt{X_0}$ that are independent of X_0, implying an insensitivity to the initial condition. By contrast, the deeper final profiles of the numerical solutions with higher B, and their scaled final runout and depth, do depend on X_0 and the initial shape. This dependence is highlighted in figure 17, which compares data for initial triangles and rectangles.

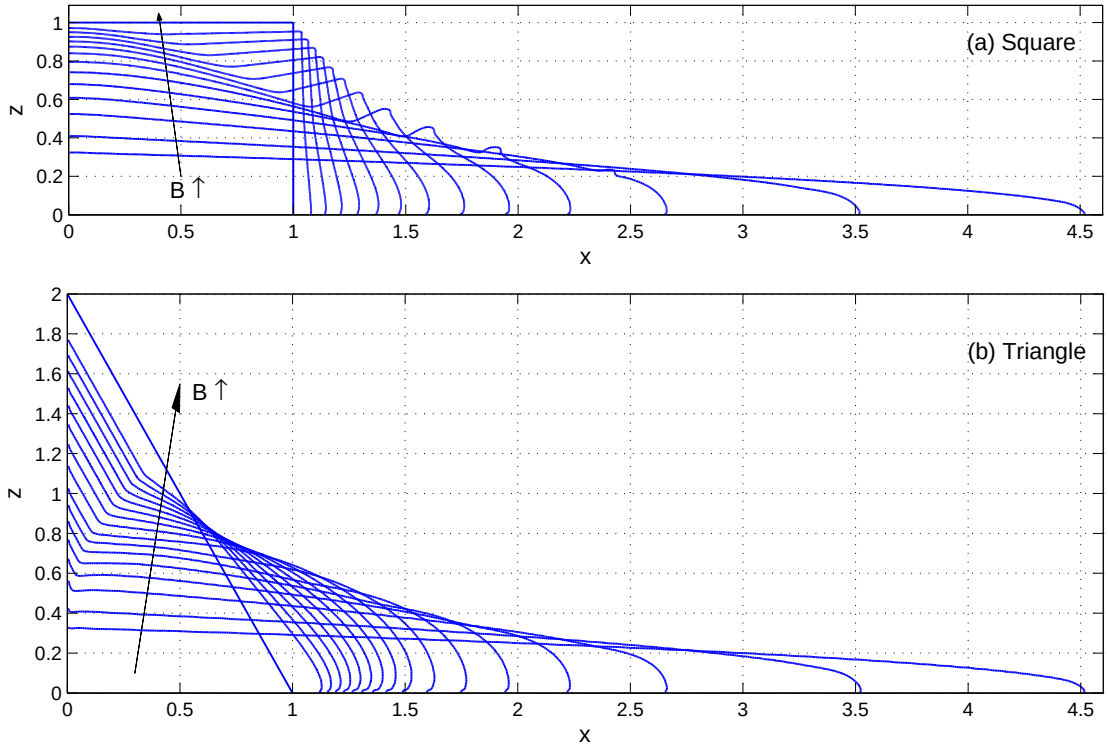

Figure 14: Profiles of the final deposit, starting from (a) a square block and (b) a triangle, with $X_0 = 1$, for $B = 0.01$, 0.02, 0.04, ..., 0.22 and 0.24, together with the initial states.

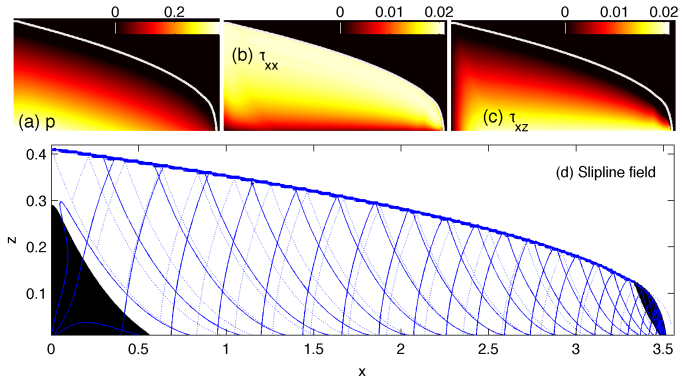

Figure 15: Final numerical solution for the slump of an initial square with $B = 0.02$, showing density maps of (a) pressure, (b) τ_{xx} and (c) τ_{xz}, and (d) the slipline field diagnosed from the numerical solution (solid) and built explicitly by integrating the slipline equations starting from the curve (9) (dotted). In (d), the plugs are shaded black, and no attempt has been made to match up the two sets of sliplines.

Figure 16 also includes data from laboratory experiments with Carbopol [17, 28] and some other fluids, which were conducted by Dubash *et al.* though not reported in their paper. None of these fluids are well fitted by the Bingham model, with a Herschel-Bulkley fit being superior. However, the final state is controlled by the yield stress and likely independent of the nonlinear viscosity of the material (at least provided inertia is not important), permitting a comparison between the experiments and our Bingham computations. Although the numerical results compare more favourably with the experiments than the slipline theory, the comparison with the leading-order asymptotic prediction is just as good. Thus, the discrepancy between theory and experiment noted by [17] is only partly due to the assumption that the slump came to rest in a state of horizontal compression, but other factors must also be at work, such as stresses in the cross-stream direction and non-ideal material behaviour. Note that the range of dimensionless yield stresses spanned by the experimental data lie well into the regime where there should be no significant dependence on the initial shape. This is comforting in view of the fact that the experiments were conducted using different initial conditions, either by raising a vertical gate or tilting an inclined tank back to the horizontal (which correspond roughly to our rectangular or triangular initial conditions).

Finally, figure 16 includes the predictions of the slender column asymptotics in (12) (see Appendix C) for $X_0 = 1$, and a formula presented by Staron *et al.* [6] based on their volume-of-fluid computations with GERRIS and a regularized constitutive law. Given that the slumps from which the data in figure 16 are taken are not slender, it is not surprising that (12) compares poorly with the numerical results. We suspect that the disagreement between our results and the fit of Staron *et al.* [6] originates either from an inadequate resolution of the over-ridden finger of less dense fluid or the significance of inertial effects in their computations. Indeed, these authors quote a final

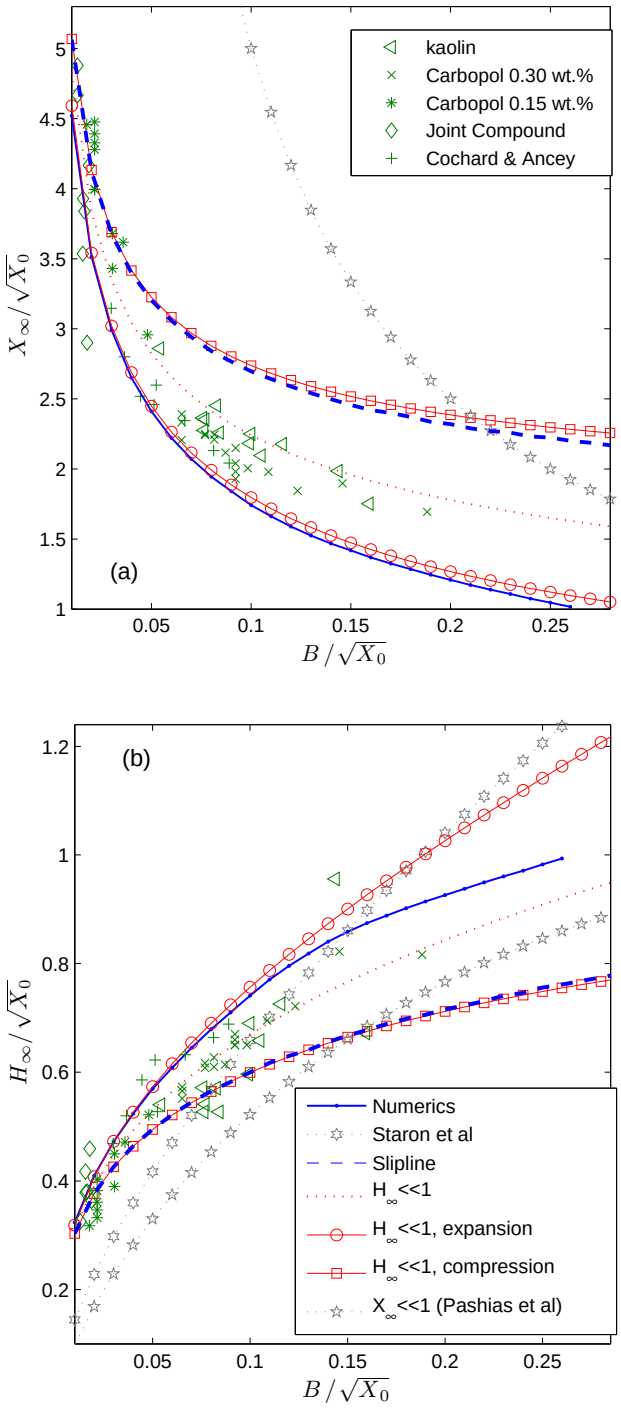

Figure 16: Scaled final (a) runout $X_\infty/\sqrt{X_0}$ and (b) central depth $H_\infty/\sqrt{X_0}$ as a function of $B/\sqrt{X_0}$ for Bingham slumps from square initial conditions (solid lines with dots). Also plotted using the symbols indicated are experimental data from [17] and [28] for slumps of aqueous solutions of Carbopol, kaolin and "Joint Compound". The leading order asymptotic prediction (8) is shown by the dotted line; the solid lines with circles or squares plot the predictions in (9) and (13); the dashed lines shows the results of slipline theory [17]. The slender-column asymptotic prediction in (12) with $X_0 = 1$ is shown by the dotted line and pentagrams. The dotted line and hexagrams show the fit proposed by Staron *et al.* [6].

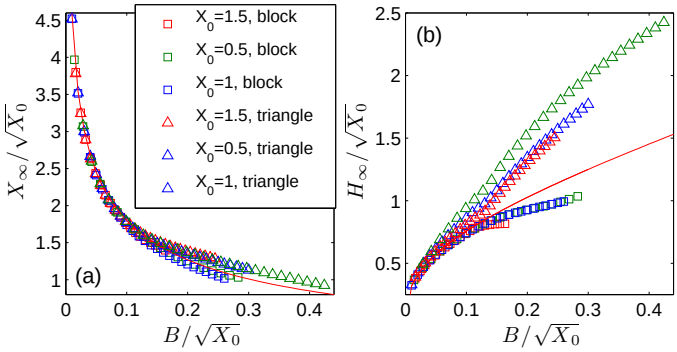

Figure 17: Scaled final (a) runout $X_\infty/\sqrt{X_0}$ and (b) central depth $H_\infty/\sqrt{X_0}$ as a function of $B/\sqrt{X_0}$ for Bingham slumps from rectangular and triangular initial conditions with $X_0 = 0.5$, 1 and 1.5. The solid lines show the predictions of the higher-order asymptotics from (9) for a complete slump.

shape that depends explicitly on the plastic viscosity of the heavier fluid, whereas this physical quantity is completely scaled out in our computations when $Re \to 0$.

5. Concluding remarks

A yield stress introduces two key features in the collapse and spreading of a viscoplastic fluid: failure occurs only provided the yield stress can be exceeded, and, when flow is initiated, the yield stress eventually brings motion to a halt. Here we have provided numerical computations of the two-dimensional collapse of Bingham fluid, exploring the phenomenology of the flow for different initial shapes. We compared the results with asymptotic theory valid for relatively shallow (low, squat) or slender (tall, thin) slumps, and with solutions from plasticity theory applying near the initiation and termination of flow. We verified that the computations converge to the asymptotic solutions in the relevant limits and identified where the plasticity solutions apply. We studied both the initial form of failure, extracting criteria for a collapse to occur, and the shape of the final deposit, comparing its runout and depth with previous experiments and predictions.

There are three key limitations of our study with regard to the collapses of viscoplastic fluids in engineering or geophysical settings. First, our two-dimensional geometry is restrictive and an axisymmetric assumption prefereable for a range of applications such as the slump test. Such a generalization raises the interesting question of how incompressible viscoplastic flow avoids the inconsistency of the von-Karman-Haar hypothesis [27]. Second, the issues associated with the no-slip condition on the underlying surface are not merely numerical: viscoplastic fluids can suffer apparent slip [29], demanding the inclusion of a slip law. Finally, inertia is important in many applications, an effect that allows slumps to flow beyond the rest states we have computed. Other interesting generalizations include the

incorporation of different rheologies, such as thixotropy, and surface tension at small spatial scales.

Acknowledgements: We thank Anthony Wachs for useful discussions. S.H. thanks NSF for support (Grant No. CBET-1554044-CAREER).

Appendix A. Further numerical notes

Appendix A.1. Parameter settings and other details

PELICANS exploits a Galerkin finite element method to solve a weak form of the equations of motion using iteration. For the regularized constitutive model, we set $\epsilon = 10^{-8}$ in (7). At each step, the regularized viscosity is computed using the velocity field from the previous step, and iteration is continued until the L_2-norm of the velocity change over the entire spatial domain falls below $10^{-6}/\sqrt{n}$, where n is the number of finite elements.

As detailed in [10], the augmented-Lagrangian method introduces additional variables to solve iteratively the weak formulation of the equations of motion whilst avoiding the singular viscosity arising at the yield surfaces and the stress indeterminacy of the plugs. The iterative scheme includes a relaxation parameter r which we select to be equal to B. Iteration is continued until the larger of the L_2-norms of the change in the velocity field or $\dot{\gamma}$ became less than $10^{-4}/\sqrt{n}$.

Based on resolution studies, we found that grids with $\Delta x = 0.01$ and $\Delta z = 0.005$ were sufficient for mesh convergence in problems for which slumps were order one aspect ratio or shallow (once the no-slip boundary condition on the base had been modified). For slender columns, we found it sufficient to take $\Delta x = 5 \times 10^{-4}$ with $\ell_x = 0.1$ and distribute the vertical mesh non-uniformly such that the grid intervals formed a geometric series starting with 5×10^{-4} at the bottom and ending at 0.005 at the top boundary $z = \ell_z = 1.1$.

Appendix A.2. The failure computation for $Re = t = 0$

For the initial failure mode, we used an alternative numerical scheme that solved the equations at $t = 0$ with $Re \equiv 0$. The scheme employed an augmented-Lagrangian method to solve the Stokes equations over the domain shown in figure 1. In view of our interest in yield stresses close to B_c, where the velocity field is small and the viscous stress of the outer fluid likely irrelevant, we simplified the computation by taking a viscosity ratio of unity.

At each step of the iteration procedure, the linear Stokes and continuity equations were converted to a biharmonic equation which was solved using a Fourier sine transform in the x direction and second-order finite differences in z. For rectangular slumps, the discontinuity in the yield stress between the two fluids was imposed directly on the finite difference grid; for triangular shaped slumps, convergence was much improved by smoothing the discontinuity over a few grid points. In both cases, the forcing term in the biharmonic equation that arises from the discontinuity in density between the two fluids was dealt with exactly in Fourier space.

As in our other scheme, the size of the domain was chosen to be sufficiently large so as to have a negligible effect on solutions (in most results, $l_z = 4/3$ and $l_x = 4X_0/3$). We selected a vertical grid and truncation of the horizontal Fourier series such that the resolution was $\Delta z = 1/999$ and $\Delta x = X_0/768$; we established that the solutions were independent of this choice. In the augmented-Lagrangian scheme, we again chose the relaxation parameter $r = B$, and the solutions were considered to be converged when the maximum change in the strain-rate invariant, $\dot{\gamma}$, had fallen below 10^{-10}.

Appendix A.3. Thickness of the over-ridden finger

For a relatively thin finger of depth $\zeta(x,t)$, flow is driven primarily by the shear stress on the interface,

$$\tau_\zeta \approx \mu_R \frac{u_\zeta}{\zeta}, \tag{A.1}$$

where u_ζ is the horizontal velocity of the interface and $\mu_R \sim \mu_2/\mu_1$ is the viscosity ratio. Conservation of mass implies

$$\frac{\partial \zeta}{\partial t} \approx -\frac{1}{2}\frac{\partial}{\partial x}\left(u_\zeta \zeta\right) \approx -\frac{\tau_\zeta}{\mu_R}\zeta\frac{\partial \zeta}{\partial x}, \tag{A.2}$$

if τ_ζ remains roughly independent of x. The shear stress τ_ζ is of order one at the beginning of a collapse and we use $\mu_2/\mu_1 = 10^{-3}$. Hence $u_\zeta/\zeta = O(10^3)$. Thus the finger effectively lubricates the overlying viscoplastic current until its thickness becomes comparable to our grid spacing ($\Delta z = 1/320$). Moreover, the solution of (A.2) then indicates that the finger thins like t^{-1}. In other words, the effective lower boundary condition on the viscoplastic current only reduces to no slip when the finger becomes difficult to resolve, and from then on, the resolution problem steadily worsens.

The critical detail of the volume-of-fluid code regarding the finger is that it treats each grid cell as a mixture with the rheology in (3) and (4) (or (7)). In the limit of low inertia, the stress state is dictated largely by the geometry of the slump and dominated by the shear stress at the base. Thus, over the bottom grid cell where $c = c_0$,

$$\frac{\partial u}{\partial z} = \frac{(\tau_{\rm xz} - Bc_0)}{c_0 + (1-c_0)\mu_R}. \tag{A.3}$$

The average horizontal speed over this cell is then

$$\overline{u}_M \sim \frac{\Delta z}{2c_0}(\tau_{\rm xz} - Bc_0), \tag{A.4}$$

if c_0 lies well away from its limits and $\mu_R \ll 1$. On the other hand, when c_0 takes such a value, the interpretation is that the interface can be contained within the lowest grid cell. In that situation, a genuine sharp interface at $0 < z = \zeta < \Delta z$, would imply

$$\frac{\partial u}{\partial z} = \begin{cases} \tau_{\rm xz} - B & \zeta < z < \Delta z, \\ \mu_R^{-1}\tau_{\rm xz} & 0 < z < \zeta. \end{cases} \tag{A.5}$$

It follows that the average horizontal speed should be

$$\overline{u}_S \sim \frac{\tau_{\rm xz}\zeta}{2\mu_R\Delta z}(2\Delta z - \zeta) \qquad \text{(A.6)}$$

for $\mu_R \ll 1$. Evidently, $\overline{u}_M/\overline{u}_S = O(\mu_R)$. In other words, when the interface enters the lowest grid cell, the treatment of the fluid as a mixture grossly underestimates the speed with which the finger will be advected horizontally; the finger is therefore not swept away fast enough, remains too thick, and overly lubricates the viscoplastic gravity current. To cure this problematic feature, the finger must be removed.

Appendix B. Shallow flow

In this and the next appendix we ignore the upper viscous fluid and consider a spreading viscoplastic current with a stress-free surface. We summarize analysis and results that are based on existing literature [4, 18], highlighting any relevant new developments; the reader is encouraged to consult the original references for additional details of the basic theory.

For relatively shallow flow (for which vertical gradients dominate horizontal gradients), the pressure becomes largely hydrostatic and only the shear stress features in the main force balance [4, 5]. Thus,

$$p = h - z \qquad \text{and} \qquad \tau_{\rm xz} = -h_x(h-z), \qquad \text{(B.1)}$$

where $z = h(x,t)$ is the position of the free surface. Here, and throughout this and the following appendices, we use subscripts of x, z and t as shorthand for the corresponding partial derivatives (except in the case of the stress components). The velocity field is now given by

$$u = -\frac{1}{2}h_x \times \begin{cases} (2Y-z)z & 0 \le z < Y, \\ Y^2 & Y \le z \le h, \end{cases} \qquad \text{(B.2)}$$

where $z = Y = h + B/h_x$ (for $h_x < 0$) is where the leading-order shear stress falls below B. This latter level is not a true yield surface because, although the overlying velocity field is plug-like, the fluid remains in extension and weakly yielded [16]. Exploiting the depth-integrated expression of mass conservation, the problem then reduces to solving the thin-layer equation [4],

$$h_t = \frac{1}{6}\frac{\partial}{\partial x}\left[(3h-Y)Y^2 h_x\right]. \qquad \text{(B.3)}$$

Note that modifications are needed where $Y = h + B/h_x < 0$, which signifies that the fluid is not sufficiently stressed to deform. This true yield criterion can be incorporated into the formulation simply by defining

$$Y(x,t) = \text{Max}\left(h + \frac{B}{h_x}, 0\right). \qquad \text{(B.4)}$$

For our triangular initial condition, with $h = 2(1 - x/X_0)$, the yield criterion indicates that the fluid will not collapse anywhere when $B > 4/X_0$; by contrast, the vertical edge of the rectangular block ensures the fluid always collapses in the shallow limit. The final state is given by $Y \to 0$, which leads to (8).

The shallow-layer theory is the leading order of an asymptotic expansion which, the current dimensionless scalings, corresponds to the limit $B \ll 1$. For the final shape one can go further with the analysis and compute higher-order corrections in the effort to extend the accuracy of the approximation. In particular, following the analysis in [17] but bearing in mind that the slump comes to rest in a state of horizontal expansion, we find

$$p \approx h - z - \sqrt{B^2 - v^2}, \qquad v = -h_x(h-z), \qquad \text{(B.5)}$$

$$\tau_{\rm xx} \approx \sqrt{B^2 - v^2} - \frac{v\tau_1}{\sqrt{B^2 - v^2}}, \qquad \tau_{\rm xz} \approx v + \tau_1, \qquad \text{(B.6)}$$

where

$$\tau_1 = -\frac{\partial}{\partial x}\left[\frac{1}{h_x}\left(v\sqrt{B^2 - v^2} + B^2 \sin^{-1}\frac{v}{B}\right)\right]. \qquad \text{(B.7)}$$

Imposing the lower boundary condition, $\tau_{\rm xz} = B$ at $z = 0$, and integrating in x then gives

$$\tfrac{1}{2}h^2 - h\sqrt{B^2 - h^2h_x^2} - \frac{B^2}{h_x}\sin^{-1}\frac{hh_x}{B} = C - Bx, \qquad \text{(B.8)}$$

where C is an integration constant. Evaluating the higher-order corrections in (B.8) (*i.e.* the second and third terms on the left-hand side) using the leading-order approximation $hh_x = -B$ leads to (9) with $C = BX_\infty - \pi^2B^2/8$.

Appendix C. Slender columns

When the column of viscoplastic fluid remains slender throughout its collapse, we may use the thin-filament asymptotics outlined by [18]. The key detail is that the horizontal gradients are much larger than the vertical ones and the vertical velocity greatly exceeds the horizontal speed. Moreover, because the sides of the column are stress free, shear stresses must remain much smaller than the extensional stresses and the vertical velocity cannot develop significant horizontal shear and remains largely plug-like. These consideration indicate that (see [18])

$$w \approx W(z,t), \qquad u \approx -xW_z, \qquad \text{(C.1)}$$

and

$$p \approx \tau_{\rm xx} = -\tau_{\rm zz} \approx B - 2W_z, \qquad \text{(C.2)}$$

the latter of which follows from the leading-order horizontal force balance (which is $(\tau_{\rm xx} - p)_x \approx 0$) and constitutive law (given $\dot\gamma \approx 2|W_z|$). The width-averaged mass conservation equation and vertical force balance then imply [18]

$$\xi_t + (\xi W)_z = 0 \qquad \text{and} \qquad \xi + 2(\xi p)_z = 0, \qquad \text{(C.3)}$$

where $x = \xi(z,t)$ is the local half-width.

The equations in (C.3) can be solved analytically by transforming to Lagrangian coordinates (a,t), where a denotes initial vertical position (*i.e.* the method of characteristics; *cf.* [30]). For the rectangular or triangular blocks, we have the initial condition $\xi(a,0) = X_0$ or $X_0(1-\frac{1}{2}a)$, respectively. The transformation then indicates that

$$\xi(a,t)\frac{\partial z}{\partial a} = \begin{cases} X_0 \\ X_0(1-\frac{1}{2}a) \end{cases} \qquad \text{and} \qquad \xi_t(a,t) = -\xi W_z. \tag{C.4}$$

Hence

$$\xi p = \tfrac{1}{2}X_0(1-a/a_*), \tag{C.5}$$

given that $p=0$ at the top of the column where $a = a_* = 1$ or 2. If the fluid is yielded, the constitutive law implies

$$p = B - 2W_z = B + \frac{2\xi_t}{\xi}. \tag{C.6}$$

After a little algebra and the use of the bottom boundary condition $z(a=0,t)=0$, we find

$$\frac{\xi(a,t)}{\xi(a,0)} = E + \frac{1-E}{2B}\left(1-\frac{a}{a_*}\right), \qquad E = e^{-t/2B}, \tag{C.7}$$

and

$$z = \frac{2a_*B}{1-E}\log\left[\frac{1-E+2BE}{(1-E)(1-a/a_*)+2BE}\right]. \tag{C.8}$$

The yield condition in this limit becomes $p < -B$, or $a < a_*(1-2B)$, which translates to

$$z < Z(t) = \frac{2a_*B}{(1-e^{-Bt/2})}\log\left[\frac{1-(1-2B)e^{-Bt/2}}{2B}\right]. \tag{C.9}$$

The column does not therefore yield anywhere when $B > \frac{1}{2}$. If fluid does yield, the base spreads out to a distance $\xi(0,t) \to X_\infty = X_0/(2B)$, and the column falls to a height $H_\infty = 2a_*B[1-\log(2B)]$. The yield condition and runout are the same for both the rectangle and triangle because, in the slender limit, all that matters is the weight of the overlying fluid. Sample solutions are shown in figure C.18.

The main failing of the slender asymptotics is that the no-slip boundary condition is not imposed: the fluid slides freely over the base, leading to the collapsed column being widest at $z=0$, whereas the fluid actually rolls over the base in a tank-treading motion (*cf.* figure 8). This failing must be remedied by adding a boundary layer at the bottom (with different asymptotic scalings). In any event, we attribute the lack of agreement between the slender asymptotics and the numerical results in figure 8 to this feature.

Appendix D. Plasticity solutions

In this appendix, we summarize slipline and bound computations based closely on existing work in plasticity theory [7, 8], emphasizing some minor generalizations for triangular initial shapes and circular failure curves. The reader is referred to [7, 8] for further details of the basic developments.

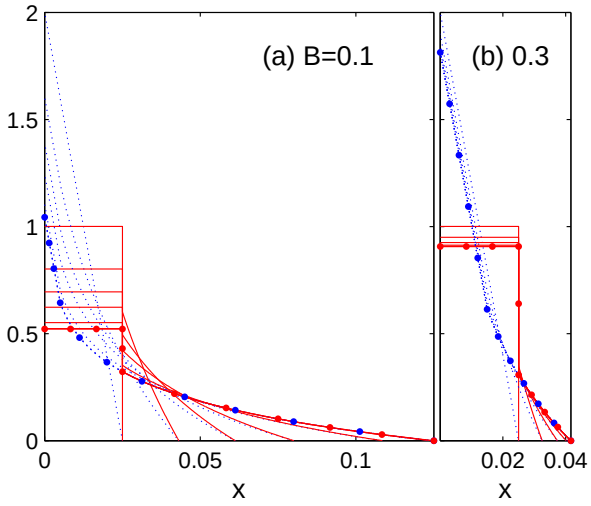

Figure C.18: Slender asymptotic solutions for (a) $B = 0.1$ and (b) $B = 0.3$, for $X_0 = 0.025$, at times $t = 0$, 4, 9, 16, 36, 100 and 1000. Collapsing rectangles (triangles) are shown by solid (dotted) lines; the dots indicate the final profiles.

Appendix D.1. Slipline fields

The slipline solutions of Chamberlain *et al.* [7] begin from the side free surface where the stress field is specified and are constructed as follows: setting

$$P \equiv \frac{p}{B} + \frac{z}{B} \qquad \& \qquad (\tau_{xx}, \tau_{xz}) = B(-\sin 2\theta, \cos 2\theta), \tag{D.1}$$

the side boundary conditions imply

$$P = 1 + \check{z} \qquad \& \qquad \theta = \frac{3\pi}{4} + \phi \tag{D.2}$$

on $\check{x} = -S\check{z}$, where $(\check{x},\check{z}) = B^{-1}(x,z)$, and $(S,\phi) = (0,0)$ for the rectangle and $(X_0/2, \tan^{-1}\frac{1}{2}X_0)$ for the triangle. On the $\alpha-$characteristics,

$$P + 2\theta = constant, \qquad \frac{\mathrm{d}z}{\mathrm{d}x} = \tan\theta; \tag{D.3}$$

for the $\beta-$characteristics,

$$P - 2\theta = constant, \qquad \frac{\mathrm{d}z}{\mathrm{d}x} = -\cot\theta. \tag{D.4}$$

Beginning from the section of the side, $0 \le \check{z} \le \check{z}_P$, with $\check{z}_P$ a parameter, the characteristics can be continued into the fluid interior using a standard finite difference scheme to solve the characteristics equations in (D.3)-(D.4) [27, 7]. Below the resulting web, an expansion fan is then added that spreads out from the base point $(x,z) = (X_0, 0)$ with $\theta_P \le \theta \le 3\pi/4 + \phi$, where θ_P is a second parameter (*cf.* figure D.19). The combined slipline field is then continued to $x = 0$, or $\check{x} = -X_0/B$. At this point, the two characteristics that bound the complete slipline field must cross and terminate with $\theta = 3\pi/4$, in view of the symmetry conditions there. This selects the two parameters $\check{z}_P$ and

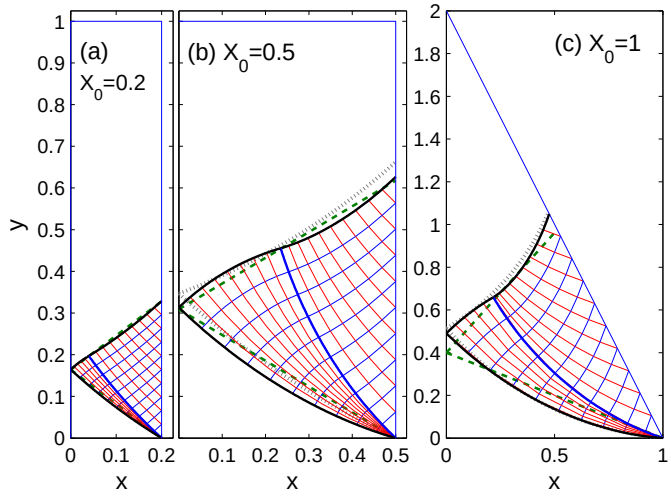

Figure D.19: Slipline solutions for a rectangle with (a) $X_0 = 0.2$ and (b) $X_0 = 0.5$, and a triangle with $X_0 = 1$. The dashed and dotted lines indicate the lower bound and its improvement of Appendix D.2.

θ_P. Finally, along the uppermost $\alpha-$characteristic, the total vertical force must match the weight of the overlying plug, which translates to imposing the condition,

$$X_0 - \tfrac{1}{2} S B^2 \check{z}_P^2 = B^2 \int_0^{\check{z}_P} \cos 2\theta \, \mathrm{d}\check{z} + B^2 \int_{X_0/B}^0 (P - \sin 2\theta) \mathrm{d}\check{x}, \tag{D.5}$$

and determines the relation $B = B_{crit}(X_0)$ (as plotted in figure 10). Examples of the slipline field are shown in figure D.19. Note that the sliplines of the two families begin to cross over one another near the top of the expansion fan if X_0 is increased past some threshold [7]. At that stage a curve of stress discontinuity must be introduced to render the slipline field single-valued. We avoid incorporating this detail here and only provide slipline solutions without a discontinuity, which limits the triangle data in figure 10(b) to $X_0 < 1$. At still higher $X_0 > 2$, the construction fails for the triangle altogether because the $\alpha-$characteristic from the base of the free surface proceeds into $z < 0$.

Appendix D.2. Simple failure modes

For the circular failure surface of a relatively wide initial rectangle, we refer the reader to existing literature (*e.g.* [24]). Here, we summarize the computation for slender rectangles and triangles.

We first consider the case where failure occurs on straight lines, as in [8]. As illustrated in figure 11(b–c), we introduce two lines of failure, with slopes $\tan\gamma$ and $\tan\zeta$, that divide the initial block up into a lower stationary triangle, an intermediate triangle that slides out sideways, and the residual overlying material that falls vertically. When the downward speed of the top is W, the continuity of the normal velocity across each failure line demands that the intermediate triangle slides out parallel to the lower failure line with velocity $U(\cos\gamma, -\sin\gamma)$, where $U = W \sec\zeta/(\tan\gamma + \tan\zeta)$. Let A_I and A_{II} denote the areas of the intermediate triangle and top block and L_I and L_{II} be the lengths of the lower and upper failure lines, both respectively. Equating the plastic dissipation across the failure lines with the release of potential energy then furnishes (in our dimensionless notation)

$$B\left(UL_I + \frac{WL_{II}\sec\zeta}{\tan\gamma + \tan\zeta}\right) = A_I U \sin\gamma + A_{II} W. \tag{D.6}$$

Geometric considerations allow us to express all the variables in terms of X_0 and the two angles γ and ζ. Equation (D.6) can therefore be formally written in the suggestive form, $B = B(\gamma, \zeta; X_0)$. We then optimize the function $B(\gamma, \zeta; X_0)$ over all possible choices of the two angles (γ, ζ) to arrive at the bound $B_c(X_0)$. It turns out that $B_c = \frac{1}{2}\tan\gamma = \frac{1}{2}\tan\zeta = \frac{1}{2}(\sqrt{1 + X_0^2} - X_0)$ for the rectangular block [8]. In the case of the triangle, $\tan\zeta = \sqrt{2(1 + \tan^2\gamma)} - \tan\gamma$, leaving a straightforward algebraic problem to solve for the optimal γ and B_c, with solutions shown in figure 11(c) and 10(b). The failure lines of these bounds are compared to the sample slipline fields in figure D.19, illustrating the manner in which the bound attempts to capture the actual plastic deformation.

The streamlines of the numerically computed failure modes suggest that the preceding bounds might be improved if the triangle at the side were allowed to rotate out of position rather than slide linearly. In this situation, the failure surfaces become circular arcs rather than straight lines which complicates the form of the power balance corresponding to (D.6) and the geometrical constraints. Three optimization parameters are required to define the circular arcs; we use the local slopes at the bottom corner, s_α, and midline, s_β and s, as illustrated in figure 11(b,c). The optimization problem can then be continued through with the help of the computer. We use the built-in function FMINSEARCH of Matlab to perform the optimization of $B(s_\alpha, s_\beta, s; X_0)$ and improve the bounds on $B_c(X_0)$. The circular failure arcs corresponding to the three slipline solutions of figure D.19 are again included in that picture.

Note that the bounds for the triangle predict that s_α falls to zero for $X_0 > 2.8$ with a straight failure surface and $X_0 > 1.2$ for rotational failure. For wider initial states, this parameter must then be removed from the optimization, which makes the bounding procedure less effective. A more general and effective construction, that retains s_α as a parameter, is to allow the lower circular failure arc to intersect the base for $x < X_0$, but not pass through that surface, and then continue beyond. That is, we allow the arc to proceed through a minimum at $z = 0$ and then intersect the side surface at a finite height (*cf.* figure 13(b,c)). This extension permits computations of improved bounds for arbitrarily wide triangles and is plotted in figure 10(b). Figure 13(b,c) illustrates how the resulting arcs compare well with the computed failure modes for

moderate width. Even for the widest triangle with $X_0 = 8$, the bound ($B_c > 0.1635$) is close to the computed value of $B_c \approx 0.1642$. For $X_0 \gg 1$, the bound converges to $B_c > 3/X_0$. By contrast, the shallow-layer asymptotics predict failure for $B_c \sim 4/X_0$ (see Appendix B), indicating that there is further room for improvement in this limit.

References

[1] N. Pashias, D. V. Boger, J. Summers, D. J. Glenister, A fifty cent rheometer for yield stress measurement, Journal of Rheology 40 (1996) 1179.

[2] N. Roussel, P. Coussot, Fifty-cent rheometer for yield stress measurements: From slump to spreading flow, Journal of Rheology 49 (2005) 705–718.

[3] N. J. Balmforth, R. V. Craster, P. Perona, A. C. Rust, R. Sassi, Viscoplastic dam breaks and the Bostwick consistometer, J. Non-Newtonian Fluid Mechanics 142 (2007) 63–78.

[4] K. F. Liu, C. C. Mei, Approximate equations for the slow spreading of a thin sheet of Bingham plastic fluid, Physics of Fluids A: Fluid Dynamics 2 (1990) 30.

[5] N. J. Balmforth, R. V. Craster, A. C. Rust, R. Sassi, Viscoplastic flow over an inclined surface, J.Non-Newtonian Fluid Mech. 142 (2007) 219–243.

[6] L. Staron, P. Lagree, P. Ray, S. Popinet, Scaling laws for the slumping of a Bingham plastic fluid, J. Rheol. 57 (2013) 1265–1280.

[7] J. A. Chamberlain, J. E. Sader, K. A. Landman, L. R. White, Incipient plane-strain failure of a rectangular block under gravity, Int. J. of Mechanical Sciences 43 (2001) 793–815.

[8] J. A. Chamberlain, D. J. Horrobin, K. A. Landman, J. E. Sader, Upper and lower bounds for incipient failure in a body under gravitational loading, J. Applied Mechanics 71 (2004) 586–589.

[9] I. A. Frigaard, C. Nouar, On the usage of viscosity regularisation methods for visco-plastic fluid flow computation, J. Non-Newtonian Fluid Mech. 127 (2005) 1–26.

[10] M. Fortin, R. Glowinski, Augmented Lagrangian Methods: Applications to the Numerical Solution of Boundary-Value Problems, North-Holland, 2006.

[11] S. Hormozi, K. Wielage-Burchard, I. Frigaard, Entry and start up effects in visco-plastically lubricated viscous shear flow in pipe, J. Fluid Mechanics 673 (2011) 432–467.

[12] K. Wielage-Burchard, I. Frigaard, Static wall layers in plane channel displacement flows, J. Non-Newtonian Fluid Mechanics 166 (2011) 245–261.

[13] B. van Leer, Towards the ultimate conservative difference scheme. V. A second-order sequel to Godunov's method, Journal of Computational Physics 142 (1) (1979) 101–136.

[14] M. Renardy, Y. Renardy, J. Li, Numerical simulation of moving contact line problems using a volume-of-fluid method, Journal of Computational Physics 171 (2001) 243–263.

[15] Y. Sui, H. Ding, P. Spelt, Numerical simulations of flows with moving contact lines, Ann. Rev. Fluid Mech. 46 (2014) 97–119.

[16] N. J. Balmforth, R. V. Craster, A consistent thin-layer theory for Bingham plastics, J. Non-Newtonian Fluid Mechanics 84 (1999) 65–81.

[17] N. Dubash, N. J. Balmforth, A. C. Slim, S. Cochard, What is the final shape of a viscoplastic slump?, J. Non-Newtonian Fluid Mech. 158 (2009) 91–100.

[18] N. J. Balmforth, N. Dubash, A. C. Slim, Extensional dynamics of viscoplastic filaments: II. Drips and bridges, J. Non-Newtonian Fluid Mech. 165 (2010) 1147–1160.

[19] N. J. Balmforth, I. J. Hewitt, Viscoplastic sheets and threads, Journal of Non-Newtonian Fluid Mechanics 193 (2013) 28–42.

[20] A. V. Lyamin, S. W. Sloan, Lower bound limit analysis using non-linear programming, Int. J. Numerical Methods in Engineering 55 (2002) 573–611.

[21] A. V. Lyamin, S. W. Sloan, Upper bound limit analysis using linear finite elements and non-linear programming, Int. J. Numer. and Analyt. Methods in Geomechanics 26 (2002) 181–216.

[22] J. Pastor, T.-H. Thai, P. Francescato, Interior point optimization and limit analysis: an application, Communications in Numerical Methods in Engineering 19 (10) (2003) 779–785.

[23] J. Heyman, The stability of a vertical cut, International Journal of Mechanical Sciences 15 (10) (1973) 845–854.

[24] W.-F. Chen, M. W. Giger, H.-Y. Fang, On the limit analysis of stability of slopes, Soils and Foundations 9 (4) (1969) 23–32.

[25] G. P. Matson, A. J. Hogg, Two-dimensional dam break flows of Herschel-Bulkley fluids: The approach to the arrested state, J. Non-Newtonian Fluid Mech. 142 (2007) 79–94.

[26] J. F. Nye, The flow of glaciers and ice-sheets as a problem in plasticity, Proc. R. Soc. Lond. Ser. A 207 (1951) 554–572.

[27] W. Prager, P. G. Hodge, Theory of Perfectly Plastic Solids, Dover; New Ed edition, 1968.

[28] S. Cochard, Measurements of time-dependent free-surface viscoplastic flows down steep slopes, Ph.D. thesis, École Polytechnique Fédérale de Lausanne (2007).

[29] M. Jalaal, N. J. Balmforth, B. Stoeber, Slip of spreading viscoplastic droplets, Langmuir 31 (44) (2015) 12071–12075.

[30] M. A. M. A. Khatib, S. D. R. Wilson, Slow dripping of yield-stress fluids, Journal of Fluids Engineering 127 (2005) 687–690.